



A soft and transparent contact lens for the wireless quantitative monitoring of intraocular pressure

Joohee Kim ^{1,2,6}, Jihun Park ^{1,2,6}, Young-Geun Park ^{1,2,3}, EunKyung Cha^{1,2}, Minjae Ku^{1,2}, Hyeon Seok An^{1,2}, Kyoung-Pil Lee⁴, Man-Il Huh⁴, Junmo Kim⁵, Taek-Soo Kim⁵, Dai Woo Kim ⁴✉, Hong Kyun Kim ⁴✉ and Jang-Ung Park ^{1,2}✉

Continuous detection of raised intraocular pressure (IOP) could benefit the monitoring of patients with glaucoma. Current contact lenses with embedded sensors for measuring IOP are rigid, bulky, partially block vision or are insufficiently sensitive. Here, we report the design and testing in volunteers of a soft and transparent contact lens for the quantitative monitoring of IOP in real time using a smartphone. The contact lens incorporates a strain sensor, a wireless antenna, capacitors, resistors, stretchable metal interconnects and an integrated circuit for wireless communication. In rabbits, the lens provided measurements that match those of a commercial tonometer. In ten human participants, the lens proved to be safe, and reliably provided accurate quantitative measurements of IOP without inducing inflammation.

Continuous physiological monitoring of the human body—via vital physical signs (for example, body temperature, heart rate and the electrical activity of the heart) and metabolites (such as glucose, lactate and alcohol) in bodily fluids (such as sweat, saliva and tears)—is essential for the diagnosis of diverse diseases^{1–13}. The eyes also provide various vital signals and continuous contact with tear fluids, so they can be potential sensing sites. A contact lens can therefore provide a wearable sensing method to monitor biological signals from an eye. One of the diseases that can be diagnosed on the basis of eye condition is glaucoma. Glaucoma is an optic neuropathy that can lead to irreversible loss of vision, IOP is the only known modifiable risk factor^{9,10}, and the only available method for treatment of glaucoma is lowering IOP. Considering the degree and type of glaucoma, the target IOP should be set and medical and/or surgical management should be implemented to reach the target IOP. Thus, after setting the target IOP, it is important to check IOP periodically to determine whether it is being controlled adequately during the treatment.

One of the main contributors to the progression of glaucoma is the highest IOP level during the night¹¹, and the IOP values fluctuate even with the eyes closed on the basis of the individual's circadian rhythm¹². The continuous and real-time monitoring of IOP is therefore essential to verify the risk factor of the glaucoma progression. Although the gold-standard medical instrument for measuring IOP is Goldmann applanation tonometry, which measures the force that is required to deform the spherical cornea to a standardized diameter¹⁴, this method is subject to time and space constraints because patients must have this measurement performed in a hospital. Despite the widespread use of home tonometry, problems can arise in the clinical judgments of IOP information at home. Most tonometers available at home require that the patient or guardian

take manual measurements. The IOP measured by the patient using home tonometry can therefore differ by 5 mm Hg compared with the IOP measured by a physician using the tonometer¹⁵. This difference of 5 mm Hg in IOP might be too large to be used practically in the clinical environment. To overcome these limitations, extensive efforts have been made recently to develop other non-invasive methods for real-time continuous monitoring of IOP, and the contact lens is a promising candidate for wearable sensing technology. This contact lens sensor, which is conformally contacted with the cornea, can detect the expansion of the corneal limbus (border of the cornea and sclera) caused by the increase in the IOP^{16,17}. Although these contact lens systems can provide promising capabilities for the measurement of IOP, there are some crucial issues that need to be solved for the realization of such contact lenses. For example, conventional sensors based on metals or semiconductors are not sensitive enough to detect the minute deformations of contact lenses caused by the fluctuations of the IOP of human eyes, that is, lens deformation of only 0.03% in tensile strain per mm Hg. Complicated circuits are also required to amplify the modest signals from these sensors by filtering out background noises¹⁸. Furthermore, the use of opaque and rigid electronic materials for the sensors, integrated circuits, metallic antennas and interconnects can block the wearer's vision or damage the surface of the cornea and the eyelid^{19–21}. Furthermore, bulky equipment is also required for signal measurements from the contact lenses, which can limit the use of these contact lenses outside of clinical settings by restricting the movements of users^{22,23}. Although light-emitting diodes integrated with a sensor inside the contact lens can indicate qualitative signals above a threshold to eliminate the need for additional bulky equipment, this method is not suitable for qualitative analysis, such as monitoring the IOP²⁴.

¹Department of Materials Science and Engineering, Yonsei University, Seoul, Republic of Korea. ²Center for Nanomedicine, Institute for Basic Science (IBS), Yonsei University, Seoul, Republic of Korea. ³School of Materials Science and Engineering, Ulsan National Institute of Science and Technology (UNIST), Ulsan, Republic of Korea. ⁴Department of Ophthalmology, School of Medicine, Kyungpook National University, Daegu, Republic of Korea. ⁵Department of Mechanical Engineering, Korea Advanced Institute of Science and Technology (KAIST), Daejeon, Republic of Korea. ⁶These authors contributed equally: Joohee Kim, Jihun Park. ✉e-mail: proector97@gmail.com; okeye@knu.ac.kr; jang-ung@yonsei.ac.kr

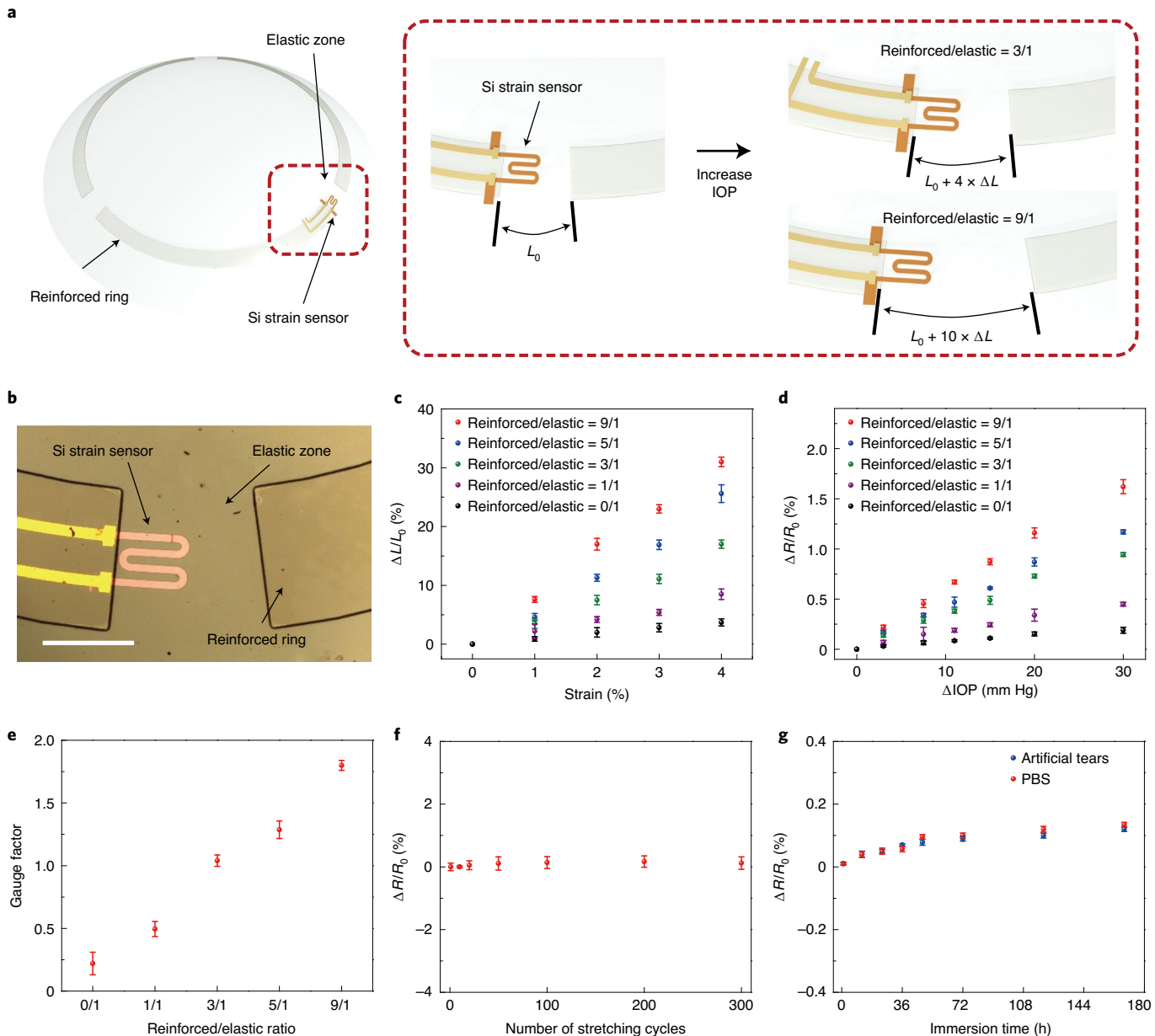


Fig. 1 | Characterizing a strain sensor on a rigid-soft hybrid layer. **a**, Schematic of the substantial concentration of the tensile strain to only the soft elastic zone when stretching the sample. The area ratio of the rigidly reinforced part to the elastic zone (reinforced/elastic) is shown. **b**, Optical micrograph of the strain sensor resting on the soft elastic zone of the hybrid film. Scale bar, 200 μm . **c**, Effective strains on the soft elastic zone along the stretching direction. The area ratio of the rigidly reinforced part to the elastic zone is shown. **d**, Relative change in resistance of the strain sensor on the hybrid layer as a function of IOP. The area ratio of the rigidly reinforced part to the elastic zone is shown. **e**, Gauge factor dependent on the area ratio of the rigidly reinforced area to the soft elastic area. **f**, The relative change in resistance of the strain sensor for 300 cycles of its stretching (up to 30% in tensile strain) and successive relaxation. **g**, Immersion test using an artificial tear solution and a PBS solution. For **c-g**, each data point indicates the average of 20 samples, and the error bars show the s.d. Each sample represents a biologically independent sample.

To overcome these limitations, in this Article, we report the fabrication of a wearable soft contact lens for the quantitative real-time monitoring of IOP using mobile phones. The contact lens is composed of a strain sensor, a strain-concentrating layer, a wireless antenna, capacitors, resistors and an integrated circuit chip, and it is designed with stretchable, electrical interconnects of three-dimensional (3D) metal structures to avoid obstructing the wearer's view. The key advantages of this lens for sensing IOP are as follows. First, material design for strain concentration, that is, a mechanically reinforced ring pattern with local narrow

disconnections is embedded inside the rim region of a soft elastic contact lens, and a strain sensor is located only in the soft elastic part between both sides of the reinforced segment. This design ensures that minute changes in the IOP can concentrate the strain to the sensor (in the elastic region) sufficiently during the deformation of the contact lens, with no need for an additional amplifier or noise-filter circuits. In contrast to previous methods that use similar rigid-soft hybrid substrates to protect ordinary electronics against mechanical deformations^{13,24–26}, in our approach, the elastic part is used to concentrate strain locally to detect fine variations of IOP. Second, a

transparent and stretchable antenna that occupies a relatively large area and has high transparency, stretchability, fine geometry and low sheet resistance (R_s) for operating a standard near-field communication (NFC) chip wirelessly at 13.56 MHz. In our approach, this transparent and stretchable antenna is formed using random networks of a hybrid nanostructure based on ultralong silver nanofibres (AgNFs) and fine silver nanowires (AgNWs). These ultra-long AgNF networks are advantageous for obtaining a low R_s with high transparency, and the fine AgNWs fill vacant areas of the AgNF networks to preserve the low resistance of fine antenna patterns, which enables reliable standard NFC (at 13.56 MHz) inside the soft contact lens. Third, stretchable integrations, that is, free-standing 3D structures of metals, are printed directly at room temperature to connect this antenna, a strain sensor and an NFC chip electrically onto the elastomeric substrate as stretchable interconnects for the soft contact lens. This formation of stretchable and free-standing 3D interconnects with high resolutions (metal diameter, 5 μm) at ambient conditions can provide miniaturized integrations that are suitable for a soft contact lens. Finally, quantitative remote monitoring, whereby the fully integrated system of this contact lens enables its wireless, battery-free operation for the simultaneous detection and transmission of IOP to a mobile phone using the standard NFC and thereby enables the diagnosis of glaucoma. The feasibility of the contact lens was examined in ten human participants. The accuracy of the lens is comparable to that of a commercially available tonometer (intraclass correlation coefficient (ICC)=0.888). Furthermore, a human pilot trial and *in vivo* tests conducted using live rabbits demonstrated the biocompatibility of the lens, as well as its safety against inflammation and thermal and electromagnetic radiation.

Results

Strain concentration. A strain sensor embedded inside a soft contact lens can detect stretching of the corneal limbus caused by the increase in IOP. An actual difference in IOP of only 1 mm Hg produces a change in the radius of the corneal curvature of approximately 3 μm (ref. 27–29), and the minute change in strain (~0.03%) caused by a 1 mm Hg fluctuation in IOP¹⁸ requires a precise and accurate strain sensor for the contact lens. Candidates for the strain-sensor materials include low-dimensional carbons (graphene, carbon nanotubes or carbon blacks), elastomers including conductive fillers, metals (including Au, Ag, and Pt) and semiconductors such as Si. Despite high gauge factors of the low-dimensional carbons, their nonlinear response to the applied strain can limit their use as IOP sensors for human eyes^{30,31}. The hysteresis behaviours of the elastomers, including conductive fillers that result from the viscoelasticity of elastomers as well as the interaction between fillers and elastomers, are also not suitable for repetitive and precise detection of IOP^{32,33}. Inorganic materials of metals or Si can offer better stability, repeatability and linearity compared with these low-dimensional carbons or elastomers³⁴. However, their intrinsically low gauge factors, especially lower gauge factors of the metals compared with the case of single crystalline Si, can be a challenge for their use as IOP-sensing contact lenses. For the enhancement of gauge factors in our approach, a mechanically reinforced ring pattern with local disconnections was embedded inside the rim of an elastic, soft contact lens to concentrate the strain mainly on the disconnected elastic zone during the deformation of the soft contact lens. As shown in Fig. 1a, a schematic of the contact lens with a red dashed box highlighting the strain sensor (Fig. 1a, left) and an expanded view of the strain sensor (Fig. 1a, right) shows the substantial concentration of the tensile strain only to the soft elastic zone of the sensor during stretching of the rim of the lens. The strain distribution of this contact lens under the application of IOP was observed using a digital image correlation (DIC) analysis (details about this measurement are provided in the Supplementary Methods). As shown in Supplementary Fig. 1, for an entirely soft

contact lens with no rigid pattern, the application of IOP dominantly induced tensile strain on the edge area of the soft contact lens (corresponding to the limbus region). The mechanically reinforced ring pattern was therefore located on the rim of our contact lens. Moreover, in the case of the contact lens (in which a rigid ring pattern with local disconnections was embedded), the strain became focused substantially on the soft, elastic area between two rigid areas (Supplementary Fig. 2). The tensile strain applied to this rigid–soft hybrid layer by mechanical stretching (corresponding to an IOP of 1 mm Hg) was calculated quantitatively using finite element analysis (FEA); Supplementary Fig. 3 shows the distribution of the strain. Here, the strain is concentrated mainly in the soft elastic area, whereas the strain on the mechanically reinforced parts is negligible. Thus, by considering this distribution of strain, a strain sensor composed of a nanomembrane of single-crystal Si in a serpentine geometry was located only on the soft elastic zone (Fig. 1b). For this design of the lens, a 50- μm -thick optical polymer (OP) layer (SPC-414; Young's modulus (E_{OP}) \approx 360 MPa) with a rigid ring pattern was embedded inside a 100- μm -thick silicone elastomeric layer (LENS) of a commercial soft contact lens material (Elastofilcon A, E_{LENS} \approx 0.09 MPa). Further details about this fabrication procedure are provided in the Methods. The substantial difference in Young's modulus between the rigid and soft parts enables the intensified stretching of the soft elastic zone, whereas negligible strain is applied to the rigidly reinforced ring while stretching this rigid–soft hybrid design of a contact lens^{24–26}. Supplementary Figure 4 presents the calculation of the areal ratio between the rigidly reinforced part and the soft elastic part. As shown in Fig. 1c and Supplementary Fig. 5, the relative change in the length of this elastic part ($\Delta L/L_0$) increases linearly with the applied tensile strain, and the slope for this linear increase of $\Delta L/L_0$ per strain in this graph becomes greater with the areal ratio of the rigidly reinforced part to the elastic zone. Compared with the case of the sole soft lens with no rigid component, the tensile strain becomes substantially concentrated only in the elastic zone by a factor of 7.87 times greater by embedding the rigidly reinforced pattern with its areal ratio of 9/1 (reinforced area/elastic area). This rigid–soft hybrid design of the contact lens ensures that minute changes in IOP can focus strain to the sensor (in the soft elastic zone) sufficiently during the deformation of this lens, with no need for an additional amplifier or noise filter circuits. Furthermore, this rigid–soft hybrid layer presents relatively good optical transmittance (~93% at a wavelength of 550 nm) with low haze (~1.6% at 550 nm; Supplementary Fig. 6a). This hybrid structure also has continuous and smooth interfaces between the rigid and soft areas (Supplementary Fig. 6b,c). For example, the root mean squared surface roughness of this hybrid layer was less than 5 nm, which was similar to the surface roughness of conventional glass slides or plastic films.

The strain sensor was fabricated using an ultrathin (thickness, ~300 nm), p-type (boron) doped single crystalline Si layer. This Si nanomembrane in a serpentine geometry served as the piezoresistive element that rested on the soft elastic zone of this hybrid layer, as illustrated in Supplementary Fig. 7. Further experimental details about this fabrication are provided in the Methods. In contrast to previous methods that used similar rigid–soft hybrid substrates to protect ordinary electronics against mechanical deformations by locating devices on the rigid zone^{24–26}, our strain sensor was positioned on the soft, elastic area where strain could be concentrated substantially rather than being positioned on the rigid part. For the measurement of IOP, preliminary tests of this Si strain sensor were conducted *in vitro* on a bovine eyeball owing to its structural resemblance to the human eyeball (Supplementary Fig. 8). The calibration between IOP and the relative change in the resistance of this sensor was linear, and it exhibited a sensitivity of 0.05% per mm Hg (when the areal ratio of reinforced/elastic area was 9/1) (Fig. 1d). For the case of the sole soft layer with no rigid component (ratio of

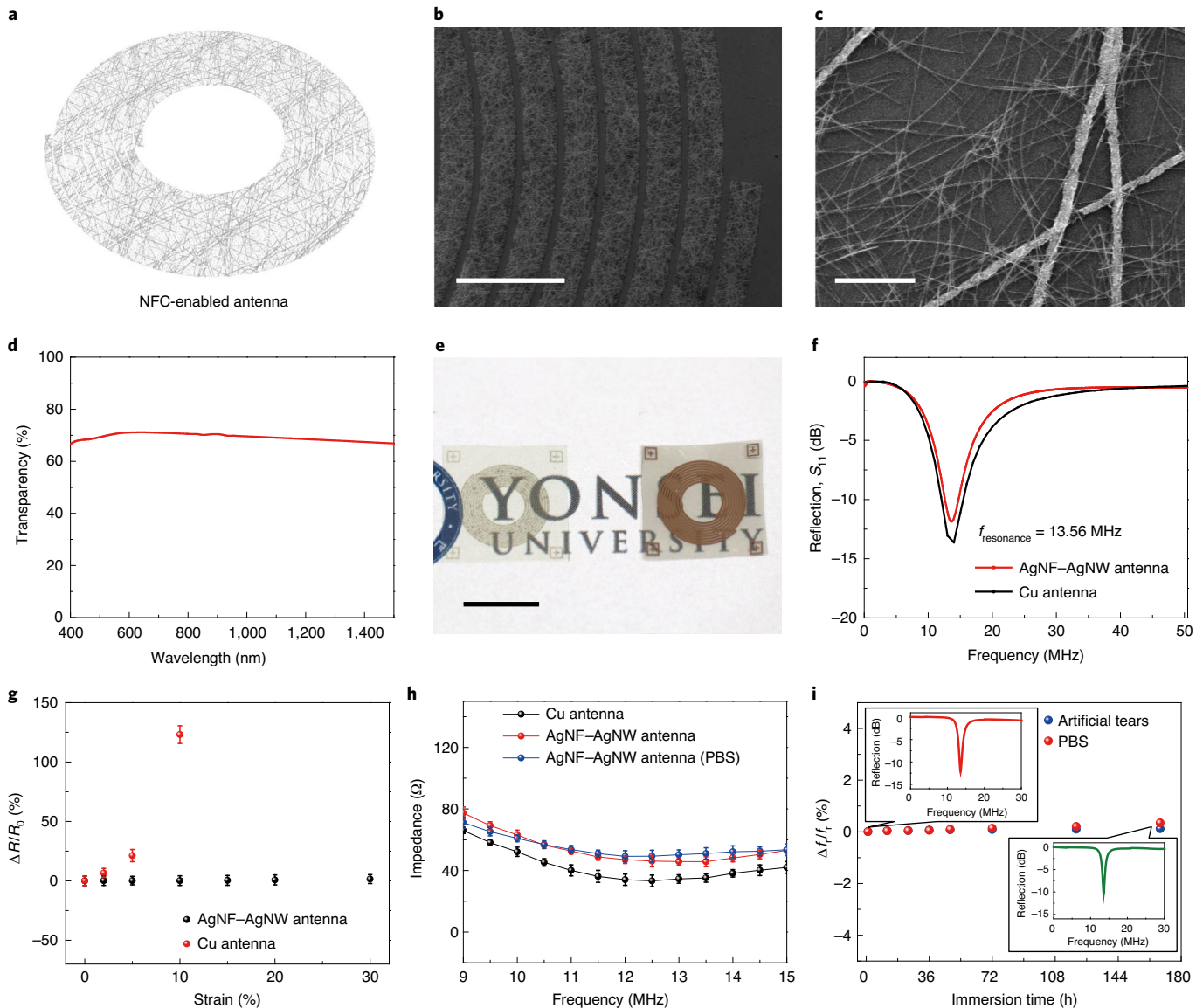


Fig. 2 | Characterization of the stretchable NFC antenna using the AgNF–AgNW hybrid networks. **a**, Schematic of the design of the antenna. **b**, SEM image of the antenna showing the pattern of the AgNF–AgNW hybrid networks. Scale bar, 1 mm. **c**, Magnified SEM image of the AgNF–AgNW hybrid structure. Scale bar, 20 μm . **d**, Optical transparency of the AgNF–AgNW hybrid. **e**, Photograph of the NFC antennas using the AgNF–AgNW hybrid (left) and Cu (right). Scale bar, 1 cm. **f**, Resonance characteristics of two antennas using Cu and the AgNF–AgNW hybrid. S_{11} is the reflection coefficient of the antenna. The resonance frequency ($f_{\text{resonance}}$) of ~13.56 MHz allows magnetic coupling. **g**, The relative change in resistance of these two antennas as a function of tensile strain. **h**, Frequency-dependent impedance of three antenna cases using Cu, AgNF–AgNW and AgNF–AgNW immersed in a PBS solution. For **g** and **h**, each data point indicates the average of 20 samples and the error bars represent the s.d. Each sample represents a biologically independent sample. **i**, Electromagnetic characteristics of the antenna in response to an artificial tear solution and a PBS solution as a function of the immersion time. $\Delta f/f_r$ is the relative change in resonance frequency ($f_{\text{resonance}}$). Insets: the electromagnetic characteristics of the antenna after immersion tests in artificial tears for 1 h (left) and 168 h (right). The individual data points represent the average of ten measurements.

the reinforced area/elastic area of 0/1), the gauge factor was measured as only 0.22, which was similar to the gauge factors of previously reported Si sensors on fully elastomeric films³⁵. However, as shown in Fig. 1e, this gauge factor, which was calculated using the overall strain applied to the entire length of the hybrid sample, increased linearly with the larger ratio of the reinforced part in the hybrid film. For example, this embedment of the rigidly reinforced zone with the reinforced/elastic ratio of 9/1 increased the gauge factor of this sensor ~8 times further and its gauge factor became as large as 1.8. This enhancement of gauge factors using the hybrid geometry enabled precise detections of IOP (Supplementary Fig. 9a).

The signal-to-noise ratio measured at 1 mm Hg was 71.75, and the minimum detectable IOP (for the case of a signal-to-noise ratio of ~3) was 0.014 mm Hg, which exceeded the 0.1 mm Hg resolution of commercially available tonometers or the levels of previously reported IOP sensors^{36–38}. Moreover, the resistance response to IOP was reproducible with negligible hysteresis (Supplementary Fig. 9b). As this ultrathin strain sensor was located on the soft elastic part of the hybrid layer, its stability against mechanical deformations was investigated (Fig. 1f). The relative change in resistance ($\Delta R/R_0$) of this sensor on the hybrid film was negligible (less than ~0.17%) even after it underwent 300 cycles of stretching (to 30% in

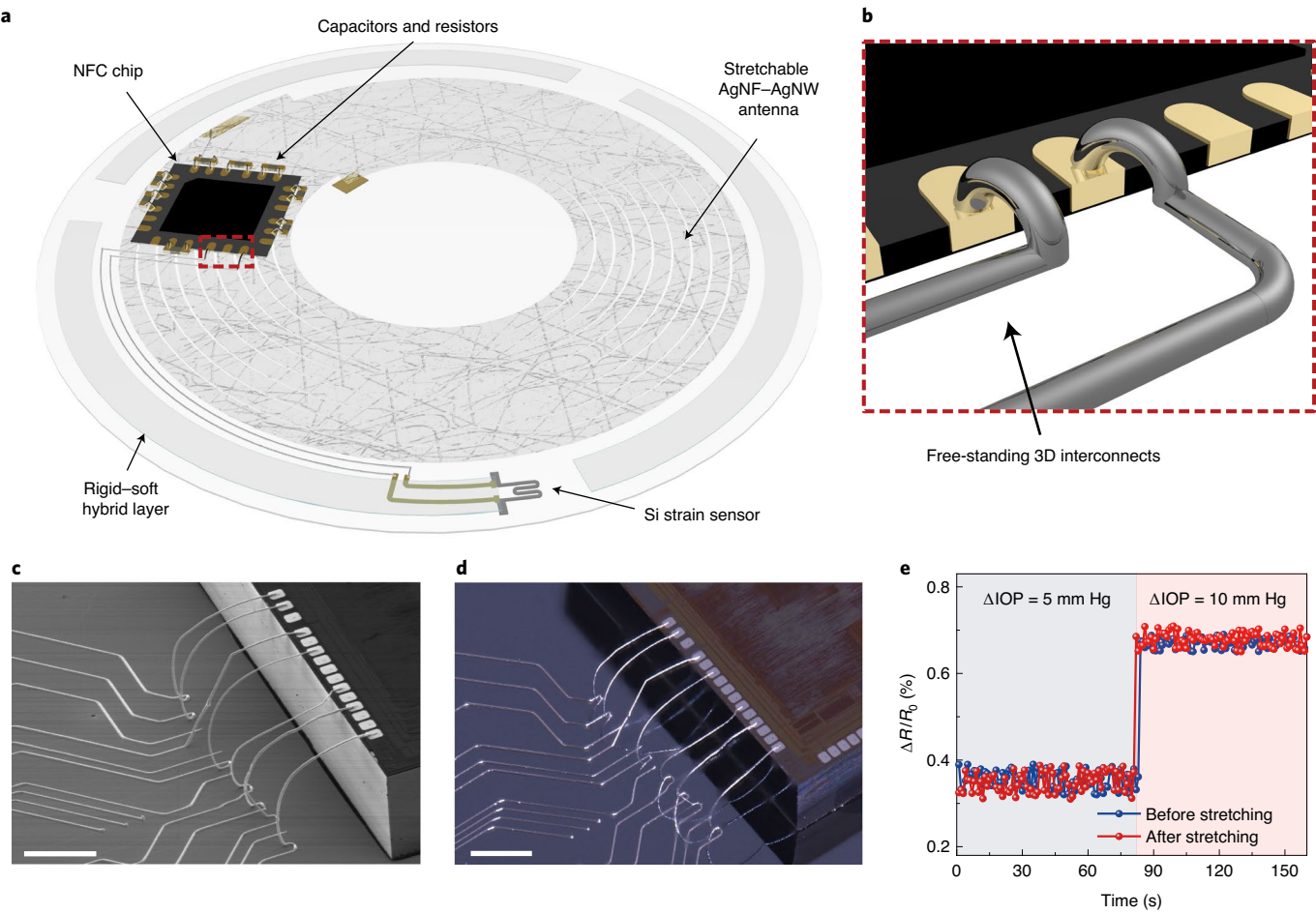


Fig. 3 | Stretchable interconnections made using direct printing of a liquid metal. **a**, Schematic of a fully integrated system, including a Si strain sensor, stretchable AgNF–AgNW antenna, NFC chip, passive elements (capacitors and resistors) and stretchable EGaN interconnects on a rigid–soft hybrid film. **b**, Schematic of the printed free-standing 3D interconnects on the metallic pads of an NFC chip. **c**, SEM image of the free-standing 3D interconnects with a line width of 5 μm for the integration of an NFC chip. Scale bar, 300 μm . **d**, Stereo zoom microscopy image of the 3D interconnects. Scale bar, 500 μm . **e**, The response of IOP from the moulded contact lens before and after stretching to 30% in tensile strain. The IOP was controlled using a syringe pump by inserting a needle into the eyeball, and a pressure sensor was inserted into the chamber of the eye to measure the IOP of this bovine eyeball.

tensile strain) and successive relaxations (here, this maximum strain value of 30% was selected because the tensile strain applied to a soft contact lens was normally less than 30% when reversing it backwards). Furthermore, no deformation of this sensor, such as wrinkling and buckling, was observed during the stretching cycles. As this strain sensor is intended for use in the contact lens, its long-term stability in tear solutions was also investigated (Fig. 1g). After storing this sensor in an artificial tear solution and in a phosphate-buffered saline solution (PBS, pH 7.4) at room temperature for 180 h, there was a negligible degradation in its response to IOP.

Wireless communication to mobile devices. As a mobile healthcare system, a contact lens requires the functionality to detect this IOP information from an eye and communicate with external mobile devices, including mobile phones, smartwatches and tablet computers wirelessly. Among standard wireless communication techniques, NFC can be attractive for the contact lens because it enables the wireless supply of the power to a sensor for its battery-free operation as well as the wireless transmission of data with sufficient bandwidth^{39,40}. In contrast to previous wireless and wearable sensors that did not include NFC chips and used high resonance frequencies in the GHz ranges^{22,41–43}, the wireless operations of the commercial NFC technology are standardized internationally for the

relatively low frequency of 13.56 MHz to avoid high crosstalk and attenuation. Thus, an antenna that occupies a relatively large area of a soft contact lens requires not only high optical transparency and good mechanical stretchability but also fine geometry and low sheet resistance (R_s) for the wireless operation of the standardized NFC chip at 13.56 MHz. However, the small size of a contact lens and the relatively high R_s of conventional transparent electrodes (such as indium tin oxide, carbon nanotubes, graphene, metal nanowires and conductive polymers) limit the design of this antenna for standardized NFC operations. In our approach, transparent and stretchable electrodes for this antenna were formed using random networks of a hybrid nanostructure based on ultra-long AgNFs and fine AgNWs. In the first step of the fabrication of the AgNF–AgNW hybrid networks, a suspension of Ag nanoparticles was electrospun continuously onto the rigid–soft hybrid film, followed by thermal annealing at 150 °C for 30 min to coalesce the Ag nanoparticles into electrically conductive AgNFs with an average diameter of 432 ± 35 nm (Supplementary Information). The single fibres were long enough to minimize the number of junctions between the one-dimensional metallic geometries, which could lead to a substantial reduction of R_s while maintaining large open spaces in the networks for high optical transparency. However, these large open areas can increase the resistance of the AgNF networks substantially

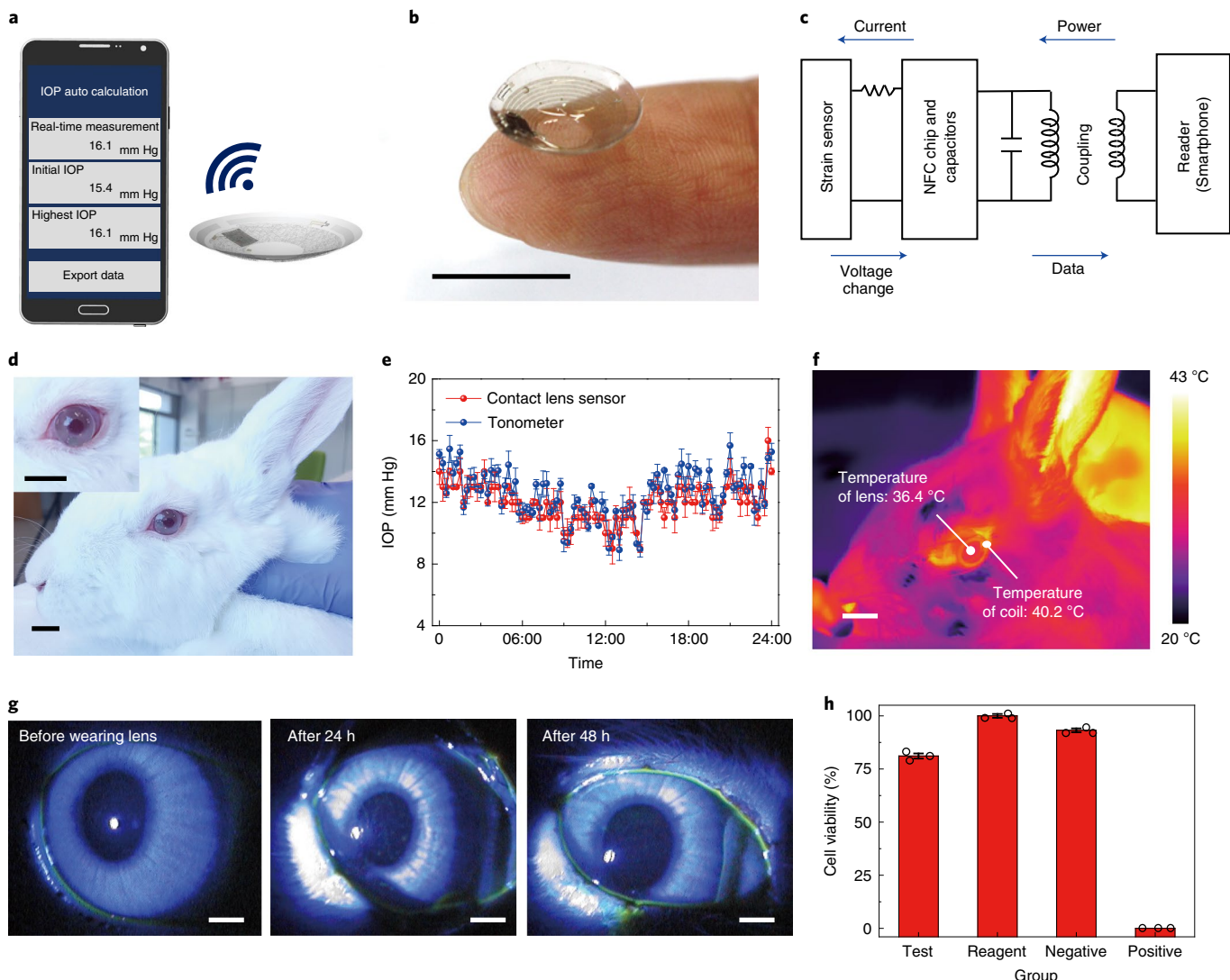


Fig. 4 | In vivo performance of the soft contact lens. **a**, Schematic of the NFC-compatible smartphone communicating with the soft contact lens. **b**, Photograph of the fabricated soft contact lens. Scale bar, 1 cm. **c**, Diagram of the integrated lens circuit. **d**, Photographs of the contact lens worn on the eye of a live rabbit. Inset: magnification of the lens area. Scale bars, 1 cm. **e**, One-day monitoring of IOP in a live rabbit using the contact lens and tonometer. Each data point indicates the average of ten measurements, and the error bars represent the s.d. **f**, Infrared image of the wirelessly operating lens worn on the eye of a live rabbit for testing heat generation. Scale bar, 1 cm. **g**, Representative series of immunofluorescence images of a rabbit's eye after wearing the contact lens for 48 h. Three images were taken. Scale bars, 0.2 cm. **h**, Cell cytotoxicity test of the contact lens. A single extract was prepared using single-strength MEM with 10% serum. After extraction, the extract was placed onto three separate confluent monolayers of L-929 mouse fibroblasts. Simultaneously, triplicates of reagent control, negative control and positive control were placed onto the confluent L-929 monolayers. The *P* values are: *P*=0.00586 (reagent), *P*=0.0139 (negative) and *P*=0.00011 (positive), determined using one-way analysis of variance. Each data point represents the average of three measurements, and the error bars represent the s.d. Each sample represents a biologically independent sample.

when they were patterned as fine geometries of the antennas with narrow widths, because locally disconnected areas were produced at the edges of the pattern by the photolithographic etching of the AgNFs. For this narrow pattern of the antenna (width, 300 μ m; space, 50 μ m) for the NFC-based contact lens (Fig. 2a), random networks of AgNWs (average length and diameter of the AgNWs, 30 \pm 5 μ m and 25 \pm 5 nm, respectively) were sprayed on top of the electrospun AgNF networks using a suspension of AgNWs. These sprayed AgNWs could bridge across the locally disconnected, open areas of the AgNF networks to preserve the resistance of these narrow antenna patterns (Fig. 2b,c). The R_s and optical transparency (at a wavelength of 550 nm) of the AgNF–AgNW hybrid networks decreased as the duration of electrospinning increased, and Supplementary Fig. 10a shows R_s as a function of the transparency

in the visible light range. As a transparent antenna for the standardized NFC operations at 13.56 MHz, the AgNF–AgNW networks formed by electrospinning of AgNFs for 10 s with successive spraying of AgNWs for 60 s. Twenty antenna samples were prepared, and their average values of R_s and transparency (at 550 nm) were $0.3 \pm 0.05 \Omega \text{ sq}^{-1}$ and $73 \pm 2.2\%$, respectively (Fig. 2d). This antenna was located outside the pupil to avoid interfering with the wearer's vision. This AgNF–AgNW hybrid structure could be patterned photolithographically to form the antenna using wet etching, and it exhibited negligible dependence of R_s on the width of patterns, and it preserved this low resistance even for the relatively narrow width of 100 μ m (Supplementary Fig. 10b). Figure 2e shows an NFC antenna with a nine-turn structure (antenna width of 300 μ m, turn space of 50 μ m) fabricated using this AgNF–AgNW hybrid

(Fig. 2e, left) and another antenna with an identical geometry of copper (Cu thickness, 500 nm; Fig. 2e, right) for comparison. This AgNF–AgNW antenna had an inductance value of $0.75 \mu\text{H}$, which could satisfy the required range of inductance from 0.3 to $3 \mu\text{H}$ for the standardized NFC operations⁴⁴. A quality (Q) factor is the frequency selectivity to a given frequency. For both antennas, that is, the AgNF–AgNW hybrid antenna and the Cu antenna, each of the coils had high Q factors of ~4.8 for the transmission distance (to a smartphone) of ~10 mm, and their resonance frequencies were centred close to 13.56 MHz for the standardized NFC condition (Fig. 2f). Compared with the brittle Cu antenna, this AgNF–AgNW antenna exhibited good mechanical stretchability with a negligible change in its resistance ($\Delta R/R_0 = 1.5 \pm 0.4\%$) under a tensile strain of 30% (Fig. 2g). The good mechanical stretchability of this antenna is suitable for a soft contact lens that needs to be turned inside out. And the total resistance of this AgNF–AgNW antenna was 38Ω , which could transfer the power from the mobiles to the contact lens under the standardized NFC condition. Higher resistance above the threshold can cause substantial power loss due to the Joule effect, which means that power can be dissipated as heat instead of electromagnetic resonance^{44,45}. To avoid the oxidation of Ag, this AgNF–AgNW antenna was passivated by coating it with a parylene elastomeric cover layer (thickness, 1 μm). Although this passivated antenna sample was immersed in a PBS solution, its resonance properties were not degraded notably, as evidenced by the impedance and phase response in Fig. 2h and Supplementary Fig. 11. Furthermore, due to this antenna's magnetic coupling at the low-frequency band (~13.56 MHz), it can communicate through biofluids with little loss for as long as 168 h after its immersion in the PBS or artificial tear solution (Fig. 2i).

Stretchable interconnections using 3D printing. Stretchable interconnects are essential to connect all of the components of the strain sensor, NFC chip, antenna and passive elements (capacitors and resistors) electrically on the rigid–soft hybrid film for a soft contact lens. Conventional interconnection techniques, such as wire bonding or flip-chip bonding, have been optimized for rigid substrates, and they are not suitable for soft and stretchable layers. Moreover, the minimum feature sizes for interconnections using these conventional methods currently are limited to the scale of ~50 μm , due to relatively large diameters of wires or sizes of solder bumps/adhesives. Further minimization for interconnections are therefore of great importance for increasing the integrity of the devices. In our approach, high-resolution direct printing of a liquid metal through a nozzle at ambient conditions was used to form stretchable 3D patterns of interconnects. In contrast to previously reported droplet stacking or instantaneous jetting methods⁴⁶, this direct printing method can generate continuous and uniform filaments of the liquid metal as stretchable interconnects. Furthermore, the use of fine nozzles facilitates the ejection of narrow metallic filaments that can be advantageous for maintaining these free-standing 3D structures by increasing the relative surface area of robust oxide skin to fluidic volume. A minimum line width of 5 μm can be printed reliably using a nozzle (inner diameter of nozzle, 10 μm), and high elasticity as well as good electrical conductivity ($3.4 \text{ S} \mu\text{m}^{-1}$) of this liquid metal enables the formation of its free-standing 3D structures as stretchable interconnects.

Figure 3a,b illustrates layouts of the contact lens system of which the Si strain sensor, AgNF–AgNW antenna coils, NFC chip, capacitors and resistors are integrated using stretchable 3D interconnects of this liquid metal on the rigid–soft hybrid layer. Here, a Si-based logic bare die (RF430FRL152H, Texas Instruments) was used as the NFC chip to capture the measured data at a high acquisition rate and then for digitizing and processing the information for transmission to the smartphone. A binary eutectic alloy of gallium and indium (EGaIn, 75 wt% Ga and 25 wt% In, Changsha

Santech Materials) was used as the liquid metal. A description of this 3D printing setup and the detailed experimental method is provided in the Supplementary Information. Coordinating the operation of the pneumatic pressure with the system of a translation stage enabled direct printing of EGaIn under ambient conditions. For example, Fig. 3c,d shows a scanning electron micrograph (SEM) and an optical micrograph of the free-standing 3D interconnects printed with a line width of 5 μm . Supplementary Figure 12a,b illustrates the layout of the device schematically, and Supplementary Fig. 12c shows an optical micrograph of the electrical connections between the NFC chip, capacitors and the antenna. Furthermore, Supplementary Fig. 12d,e presents the magnified images of the interconnects between the NFC chip and the antenna, and between the NFC chip and the strain sensor, respectively. The SEM image in Supplementary Fig. 12f shows the 3D structure of these connections between the NFC chip and capacitors. Here EGaIn was printed to contact with metal pads of the NFC chip and the other device components directly, which made the additional soldering process unnecessary. The high stretchability of EGaIn prevented the breakage of these 3D interconnects or their contact with the metal pads during deformations of the resulting contact lens. After 3D printing of EGaIn, the top surface of the printed sample was additionally encapsulated by vacuum deposition of a 500-nm-thick parylene elastomeric cover layer to prevent damage from the tear fluid. This parylene encapsulation layer is stretchable and can protect the underlying device components with 3D interconnects. Subsequently, after injecting a precursor of silicone elastomer (a commercial soft-lens material), this flat and stretchable sample was moulded into the shape of a contact lens (Supplementary Fig. 13). Thus, these fully integrated components were embedded inside a soft contact lens to prevent them from coming into physical contact with tears. Owing to the outstanding stretchability of these 3D interconnects, this moulded lens had a stable IOP sensing performance with negligible degradation of sensitivity, even after mechanical stretching up to 30% in tensile strain (Fig. 3e).

In vivo studies using a contact lens. Figure 4a,b presents a schematic and photograph of this fully integrated contact lens for monitoring IOP in glaucoma by wirelessly transmitting data to a mobile phone through the standard NFC interface. This contact lens prevents interference with the wearer's field of vision because all of the components are placed outside the wearer's pupil. Supplementary Fig. 14 describes the overall fabrication processes for this contact lens, and Fig. 4c illustrates the entire circuit system, which consists of the integration of the strain sensor, resistor, capacitor, NFC chip and its antenna for wireless communication to a reader (an NFC-compatible smartphone). The smartphone wirelessly delivers the power for operating the logic chip by providing the alternating current bias required to evaluate the sensor's response. This logic chip with a 14-bit analogue-to-digital converter provides all of the computing functionality required for both recording high-speed data and the real-time, wireless transmission of the sensor's output. Before wearing this contact lens, the initial value of the IOP needs to be measured first using a tonometer according to the clinical standard protocol. After wearing this contact lens, the change in the IOP can be monitored in real time through the automatic calibration in the software of a smartphone (further details about the calibration for the IOP readout are provided in the Supplementary Methods). In particular, this NFC chip also includes a thermoresistive sensor that provides the ability to detect temperature (T) in the range of 0–70 °C. The values of both IOP and T that are detected from the strain sensor and the temperature sensor are transmitted separately to the smartphone through NFC. The resistance of Si increases linearly with T , so the temperature-dependent change in the resistance of the Si can be calibrated according to a specific calibration equation

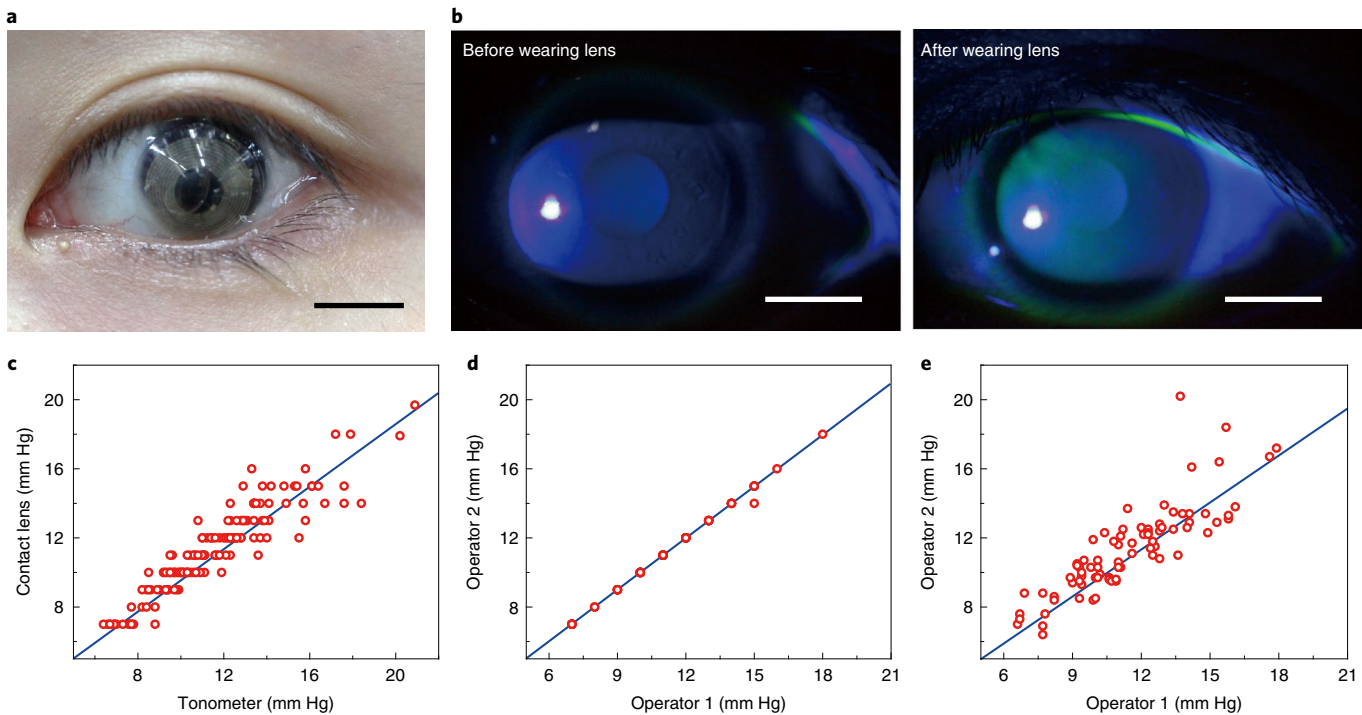


Fig. 5 | Human study of the soft contact lens. **a**, Representative photograph of the human eye with the contact lens. Ten images were taken. All of the images taken are provided in Supplementary Fig. 24. Scale bar, 1 cm. **b**, Representative series of immunofluorescence images of the human eye before and after wearing the contact lens for 12 h. Ten images were taken. All of the images taken are provided in Supplementary Fig. 24. Scale bars, 0.5 cm. **c**, Correlation between the IOP measurements taken using the contact lens and the tonometer. **d**, Interoperator reproducibility of the contact lens for IOP measurement. **e**, Interoperator reproducibility for the tonometer.

to improve the accuracy of the strain measurement (Supplementary Fig. 15a and Supplementary Methods). After coding this calibration equation in the software of the smartphone, the IOP value measured from the strain sensor can be calibrated automatically against the temperature variation (Supplementary Fig. 15b).

The IOP values measured from this contact lens were compared directly with the pressure assessed by manometry. To exclude variables that could affect IOP such as the eye movement or heartbeat, the rabbit's enucleated eye was used for this manometry test, and two fine needles (26 gauge) were inserted into the eye to apply and assess the pressure (Supplementary Fig. 16a). Our contact lens device also was placed on this eye to detect IOP simultaneously using both the contact lens and the manometry test (Supplementary Fig. 16a, bottom left inset). Then, pressure was applied using a syringe to increase the IOP of this eye. Subsequently, the IOP of this eye was decreased by reducing the pressure. Supplementary Figure 16b shows that the IOP values measured using this contact lens were correlated with the manometry cases, presenting good reproducibility and negligible hysteresis.

Figure 4d and Supplementary Fig. 17 show photographs of a live rabbit wearing this contact lens for the *in vivo* recording of IOP. As shown in Supplementary Video 1, the IOP value calibrated with this temperature dependence could be recorded wirelessly using a mobile phone. To evaluate the performance of the contact lens, a live rabbit was used for a direct comparison of the IOP measured by our contact lens sensor and the manometry. For this experiment, the rabbit's eye was cannulated using two needles (26 gauge). Supplementary Fig. 18a shows that one arm of the needle was connected to the manometry, and the other arm was connected to an adjustable reservoir of aqueous PBS solution. The rabbit also was wearing the contact lens, which completed the initial calibration step. Next, our contact lens and the manometry detected the

IOP simultaneously while pressure was being applied with a syringe (Supplementary Fig. 18b). Supplementary Figure 18c shows that the IOP values measured using our contact lens were correlated to the manometry cases. As shown in Fig. 4e, the profile of the rabbit's IOP was measured by wearing this contact lens on its eye at 15-min intervals for 24 h (recorded using a smartphone), and the profile was then compared with the IOP value detected in the same eye using a commercially available tonometer (ICare Pro, ICare). These fluctuation profiles of IOP obtained from the contact lens and the tonometer exhibited similar tendencies. For example, for both measurements, IOP was reduced between 05:00 and 10:00 and then it increased gradually between 19:00 and 23:00. The lowest and highest values of IOP were recorded around 12:00 and 23:00, respectively. Generally, the IOP values measured during the daytime were lower than the values measured at night.

To determine whether there was any undesired damage to the eye due to the eye's exposure to the heat produced by the electronic devices, the generation of heat was monitored using an infrared camera during the wireless operation of this lens (Fig. 4f and Supplementary Video 2). While the rabbit was wearing this operating lens circuit, the temperature was maintained at ~36.4 °C with negligible fluctuation of heat due to its magnetic coupling at the relatively low-frequency band (13.56 MHz). Although the wireless power transfer from the transmitting coil to the lens increased the temperature of the transmitting coil to ~40.2 °C, which was slightly higher than the temperature of the surroundings, its wireless function prevented this coil from touching the rabbit's eye or eyelid with a gap of ~5 mm. Here, this metal coil was used for the wireless transmission of power to the antenna of our contact lens through the air gap of 5 mm, as illustrated in Supplementary Fig. 19. Furthermore, according to the simulation results for specific absorption rate for

a person, the maximum specific absorption rate value of our contact lens was only 0.112 W kg^{-1} (Supplementary Fig. 20), which was about 20 times smaller than the regulation value (2 W kg^{-1})⁴⁷. To investigate the long-term stability of this contact lens, the accelerated aging test⁴⁸ was performed at an aging temperature of 65°C . For this test, our contact lens device was stored in an artificial tear solution for up to 5 d and also in PBS solution (pH 7.4) for up to 23 d, corresponding to a wearing time of 1 month and a storage period of 1 year. Next, our contact lens device was placed onto the extracted eyeball of a rabbit before operating this device by applying an IOP of 10 mm Hg (further details about this measurement are provided in the Supplementary Methods). As shown in Supplementary Fig. 21, our contact lens device operated reliably with negligible degradations against this accelerated aging.

As an *in vivo* test of the biocompatibility of this lens system, a slit lamp examination was performed for the rabbit's eye, on which this lens was worn for 24 h or 48 h. The results of this examination indicated that the contact lens could be worn for 48 h with negligible harmful effect to the eye. Figure 4g shows that the representative fluorescence images exhibited no overt reaction by the cornea to this lens. Furthermore, the cytotoxicity of this contact lens was tested by measuring the viability of cells from mouse fibroblasts. Extracts of this contact lens were prepared using a minimum essential medium (MEM) with 10% serum. The mouse fibroblast cells were then exposed to this extracted solution at $37 \pm 1^\circ\text{C}$ in the presence of $5 \pm 1\%$ CO₂ for 48 h, and the survival rate of cells was recorded. Figure 4h shows that the cell viability was 81%, which was comparable to the cases of commercially available soft contact lenses that included no electronic devices. It is therefore unlikely that the contact lens used to monitor IOP would be cytotoxic to humans.

Human medical studies using a contact lens. Figure 5a, Supplementary Fig. 22 and Supplementary Video 3 present a 28-year-old female human participant wearing this contact lens that enabled real-time wireless monitoring of IOP using a mobile phone. After wearing this lens for 12 h, a slit lamp examination was conducted for the participant's eye. Figure 5b shows that the representative fluorescence images indicated no overt reaction of the 28-year-old female human cornea to this lens. The conjunctival area of the participant's eye was also examined before and after 12 h of wearing the contact lens. No conjunctival injection was observed after wearing the contact lens for 12 h (Supplementary Fig. 23). Furthermore, Supplementary Fig. 24 shows all of the photographs of slit lamp examination of both eyes (left eye and right eye) from ten human participants. Furthermore, on the basis of the obtained photographs, the grades of both physical damage to human cornea and conjunctival injection were quantified using the clinical grading scale⁴⁹. This scale presents the degree of physical damage (to the cornea) and conjunctival injection level by indicating a numerical rating scale. As shown in Supplementary Fig. 25a,b, the changes in average corneal fluorescein stain score and conjunctival injection level after wearing the contact lens sensors were less than 0.3 and 0.2, respectively, and there were no statistical differences between before and after wearing contact lens. These results indicated that the physical damage to human cornea and conjunctival injection were negligible after wearing the contact lens. Furthermore, the visual analogue scale (VAS) was investigated for ten human participants after they had worn our contact lens for 12 h. The VAS presents their pain levels while wearing the contact lens by indicating a numerical rating scale (no pain, 0; worst pain, 10). As shown in Supplementary Fig. 26, the average VAS score was less than 2, which indicated that the NFC chip did not cause any substantial discomfort to the human eye.

The precision and accuracy of this contact lens were evaluated and compared with the gold-standard IOP measurement using a

tonometer. For this purpose, the intrasession repeatability, inter-session reproducibility and interoperator reproducibility of this lens for the measurement of IOP in human eyes of ten participants were studied. Supplementary Table 1 presents the mean IOP values, within-participant standard deviation (S_w), coefficient of variation (CV_w) and precision for intrasession repeatability. The low S_w with a small precision range indicates excellent intrasession repeatability of the contact lens and the tonometer for measuring IOP. Figure 5c shows the intersession reproducibility between the contact lens and the tonometer. For this characterization, IOP values were measured for both eyes of ten different participants, and the eyes of each participant were measured six times per day for 4 d using both the tonometer and contact lens device. In the human measurements, the IOP values were first measured using our contact lens. Immediately after removing the contact lens, the IOP was subsequently measured using the tonometer. Moreover, the IOP values from ten human participants were measured using the rebound tonometer, before and during wearing the contact lens and after removing the lens. These measurements were conducted within 5 min per person. As shown in Supplementary Fig. 27, the wearing or removal of the contact lens changed IOP negligibly, which is consistent with a previous study in demonstrating that the wearing and removal of the contact lens has a negligible effect on the human IOP⁵⁰. These two different ways of measuring IOP, that is, using either the lens or the tonometer, had a strong correlation ($ICC = 0.888$) with the coefficient of determination (r^2) of 0.808, which indicated a good intersession reproducibility for both IOP measurements. The interoperator reproducibility was calculated by means of the ICC, and this lens measurement exhibited higher ICC values ($ICC = 0.999$, $r^2 = 0.998$) compared with the tonometer case ($ICC = 0.854$, $r^2 = 0.732$) (Fig. 5d,e). More details about the statistical analysis for these measurements are provided in the Methods. These results indicate that this contact lens permitted more independent operations than the tonometer measurement, which could have been influenced by the skill levels of the operators. Supplementary Figure 28 shows the variation of the IOP for all of the participants as a function of time. The IOP values fluctuated slightly during the measurement period (4 d) in a manner that is similar to the range of variation reported previously⁵¹. For further information about the human participants, the data obtained from the ten human participants are provided in Supplementary Dataset 1.

Discussion

We developed a soft contact lens that can monitor the IOP of human eyes in real time using a mobile phone to diagnose the progression of glaucoma. To measure IOP, a strain sensor was located on the elastic zone where strain can be largely concentrated using the modulation of Young's modulus. Electronic circuits for NFC with stretchable and high-resolution interconnections were fully integrated in the lens, enabling wireless and battery-free operation. The human pilot trial and *in vivo* studies conducted using live rabbits showed the good biocompatibility of the lens, with accuracy comparable to gold-standard tonometry. Furthermore, the lens showed good stability against inflammation as well as thermal and electromagnetic radiation, its negligible corneal abrasion. The soft contact lens may offer a non-invasive mobile healthcare solution for the monitoring of IOP in patients.

Methods

Preparation of the rigid–soft hybrid film for strain concentration. For the preparation of the rigid–soft hybrid film, a LOR 3A sacrificial layer (thickness, 300 nm; MicroChem) was spun on a Si wafer. Subsequently, an elastomer (Elastofilcon A, CooperVision) mixed with a base and a curing agent using a weight ratio of 10:1 was spin-coated (5,000 r.p.m. for 5 min) and thermally cured at 100°C for 1 h (film thickness, 5 μm). Next, an OP (SPC-414, EFiRON) was spun (1,500 r.p.m. for 30 s) for a thickness of 50 μm and then photolithographically patterned as the rigid ring structure. The entire structure was covered with the elastomeric layer by spinning

(1,000 r.p.m. for 30 s; the thickness of 100 µm) and thermally curing at 100 °C for 1 h. In the last step, the sacrificial layer was removed by mr-Rem 700 (Micro Resist Technology) to delaminate the hybrid film from the Si wafer.

Fabrication of the Si-nanomembrane strain sensors. The process was initiated by the highly p-doping process on a silicon-on-insulator (SOI) wafer (Soitec, unibond with a 300-nm-thick top Si layer (p-type) with a resistivity of 14–22 Ω cm and a 400-nm-thick buried oxide layer) using impurity diffusion. Boron was predeposited in a furnace at a temperature of 1,050 °C for 70 s in a flow of N₂ (1,000 standard cm³ min⁻¹) using the rapid thermal annealing process to diffuse boron uniformly across the 300-nm-thick top Si layer. After patterning the top Si layer for the structure of the strain sensor using reactive ion etching (RIE), this Si pattern was transferred onto a target substrate by etching away the buried oxide layer of the SOI wafer using a 50% HF solution and picking up the etched Si pattern using a poly(dimethylsiloxane) (PDMS, Sylgard 184, Dow corning) stamp. After this transfer process, electrodes (thicknesses of Cr/Au, 3/200 nm) of the strain sensor were deposited and patterned photolithographically.

Optical characterization. The optical transparency of samples was measured using a ultraviolet-visible–near infrared spectroscopy (Agilent, Cary 5000 UV-Vis-NIR). The transparency of the substrate was excluded.

Electrical characterization. The electrical characteristics of the Si strain sensor were determined using a probe station (Keithley 4200-SCS). The real-time sensing of this Si strain sensor was conducted with a drain voltage (V_D) of 0.7 V.

Bovine eyeball experiment. In vitro tests were performed using a bovine eyeball. The IOP of this eyeball was controlled using a syringe pump by inserting a needle into the eyeball. And a pressure sensor (Testo 511, Testo) was inserted into the chamber of the eye to measure the IOP of this bovine eyeball. The change in the resistance of the strain sensor was characterized using a probe station (Keithley, 4200-SCS).

Fabrication of the antenna using AgNF–AgNW networks. For the formation of ultralong AgNFs, a suspension of Ag nanoparticles (NPK; average diameter, 40 ± 5 nm; solvent, ethylene glycol; concentration, 50 wt%) was electrospun continuously onto the target substrate. The distance between the nozzle and the substrate was 21 cm. The direct current bias applied to the nozzle tip was 8 kV, and the inner and outer diameters of the nozzle were 0.34 and 0.64 mm, respectively. The temperature and relative humidity were 17 °C and 4%, respectively. Subsequently, the electrospun sample was thermally annealed at 150 °C for 30 min to coalesce the Ag nanoparticles into electrically conductive AgNFs (average diameter of 432 ± 35 nm). Next, a suspension of AgNWs (Nanopyxis, average AgNW diameter, 30 ± 5 nm; average length, 25 ± 5 µm) was electrosprayed onto the electrospun AgNF sample to fill the empty spaces between AgNFs (electrospray duration of 1 min). These AgNF–AgNW structures were patterned photolithographically using a wet etching process for the antenna.

Wireless electromagnetic characterization. Wireless communication properties (for example, resonance frequency, impedance, phase, Q factor) were characterized using a network analyzer (Rohde & Schwarz, ZNB 8). For immersion tests of the antenna, the characteristics of the antenna were measured after immersing the antenna sample in an artificial tear or PBS solution.

Printing the stretchable interconnect. The direct-printing system consisted of a nozzle connected to an ink reservoir, a pneumatic pressure controller and a five-axis stage with automatic movements in the x, y or z axis and two tilting axes in the x–y plane. The nozzles were prepared using a pipette puller to make glass capillaries with desired inner diameters. For printing, a nozzle was mounted onto a syringe-type reservoir, and the rigid–soft hybrid film was placed on the five-axis stage. After delivering the EGaIn ink (75.5% gallium, 24.5% indium alloy by weight) from the reservoir to the tip of the nozzle to form a pendent ink using the pressure pump, the separation between the nozzle tip and the substrate was controlled at 2–16 µm for printing. Coordinating the operation of the pneumatic pressure with the system of a translation stage enables direct printing of the liquid metal ink under ambient conditions. Printing was performed at 30 p.s.i., and the printing velocity was controllable up to 0.2 mm s⁻¹. For 3D printing, the stage moved in the z direction at 0.001–0.01 mm s⁻¹ while applying 3 p.s.i. to the ink. To finish the printing and cut off the line, the stage moved in the z direction at 0.5 mm s⁻¹, applying no pressure to the ink.

Embedding of the integrated wireless circuit into a soft contact lens. After fabricating the fully integrated circuit and sensor on the rigid–soft hybrid layer, the sample was placed onto a mould to form a contact lens. In our experiments, we fabricated two differently sized contact lenses (one for the rabbit eye and one for the human eye). After scanning the size of each eye using a commercial 3D scanner (RESCAN DS2, Solutionix), moulds for these eyes (radius, 7.0 mm (rabbit eye) and 8.0 mm (human eye)) were formed using aluminium metal to produce soft contact lenses. Except for their sizes, these two different lenses (one for the rabbit and one for human) had identical structures. Subsequently, this mould and the device sample was filled with the elastomer (soft contact lens material) before thermal curing at 100 °C for 1 h. After moulding, the resulting contact lens was detached from the mould.

Rabbit experiments. All in vivo studies were conducted according to the guidelines of the National Institutes of Health for care and use of laboratory animals and with the approval of the Institute of Animal Care and Use Committee of UNIST, and the Institute of Animal Care and Use Committee of Yonsei University (UNISTIACUC-18-02 and IACUC-A-201908-945-02). The Institute of Animal Care and Use Committee of UNIST and the Institute of Animal Care and Use Committee of Yonsei University are the ethics review committee.

Slit lamp examination using rabbits. After removing the worn contact lens, a droplet (volume, 2 µl) of 2% fluorescent dye was applied to the lower conjunctival sac to evaluate the ocular surface with a slit lamp (SL-15, Kowa Optimed). In the case of the experiments with rabbits, this examination was performed after the lens had been worn for 24 h and 48 h. The study was approved by the Institutional Animal Care and Use of Committee of Daegu-Gyeongbuk Medical Innovation Foundation (DGMIF), and it was performed in accordance with the protocols approved by the Institutional Animal Care and Use of Committee (DGMIF-18041703-00).

Slit lamp examination in a human study. The protocol for this study was approved by the Institutional Review Board of UNIST (UNISTRB-18-17-A) and the participant gave informed consent. The contact lens was rinsed using a commercially available cleaning solution for contact lens (Frenz-pro B5 solution, JK Pharmaceutical), followed by additional rinsing using a PBS solution for 1 min before wearing. This examination was performed after the lens had been worn for a duration of 12 h. After the human trial, the ocular surface of the volunteer was evaluated using the slit lamp examination (SL-15, Kowa Optimed). The authors affirm that human research participants provided written informed consent for the publication of the images in Fig. 5, Supplementary Figs. 22–24 and Supplementary Video 3.

Statistical comparison between the measurement of the contact lens and the tonometer for sensing IOP. The reliability of the contact lens was characterized by its repeatability and reproducibility. For this comparison, the Bland–Altman method was used. The 95% limits of agreement with 15% discordance rate were calculated as a mean difference of ±1.96 from the s.d. According to the method, the 95% interval of within-participant s.d. (S_w) was related to the number of observations and participants by equation (1):

$$15\% \times S_w = 1.96 \times \frac{S_w}{\sqrt{2n(m-1)}} \quad (1)$$

where n and m are the numbers of observations and participants, respectively.

From equation (1), the number of observations and participants can be calculated using equation (2):

$$n = \frac{1.962}{2(m-1) \times 0.152} \quad (2)$$

In our study, n and m were 6 and 20, respectively. Therefore, the IOP of 10 normal participants was evaluated using the contact lens and the tonometer on both eyes. Two operators consecutively measured IOP for 4 d, and both eyes were measured six times each day. Each eye was measured using the contact lens and subsequently using the tonometer by two operators.

After completing these IOP measurements, all of the parameters, including S_w precision (repeatability coefficient, $1.96 \times S_w$), coefficient of variation (CV_{w} , $100 \times S_w/\text{overall mean}$) and ICC were calculated using Excel and SPSS. A high ICC value close to 1 indicates high similarity between the measurements from the same group.

Reporting Summary. Further information on research design is available in the Nature Research Reporting Summary linked to this article.

Data availability

The rabbit in vivo data are available at Figshare (<https://doi.org/10.6084/m9.figshare.13289342>)⁵². The human data are available within the paper and its Supplementary Information. The raw and analysed datasets generated for the studies shown in Figs. 1–3 are available for research purposes from the corresponding authors on reasonable request.

Received: 26 June 2019; Accepted: 22 March 2021;

Published online: 3 May 2021

References

- Yang, X. et al. Bioinspired neuron-like electronics. *Nat. Mater.* **18**, 510–517 (2019).
- Xu, S. et al. Soft microfluidic assemblies of sensors, circuits, and radios for the skin. *Science* **344**, 70–74 (2014).
- Dai, X., Zhou, W., Gao, T., Liu, J. & Lieber, C. M. Three-dimensional mapping and regulation of action potential propagation in nanoelectronics-innervated tissues. *Nat. Nanotechnol.* **11**, 776–782 (2016).

4. Zhang, K. et al. Origami silicon optoelectronics for hemispherical electronic eye systems. *Nat. Commun.* **8**, 1782 (2017).
5. Anwar, T. et al. p38-mediated phosphorylation at T367 induces EZH2 cytoplasmic localization to promote breast cancer metastasis. *Nat. Commun.* **9**, 2801 (2018).
6. Gao, W. et al. Fully integrated wearable sensor arrays for multiplexed in situ perspiration analysis. *Nature* **529**, 509–514 (2016).
7. Kim, D.-H. et al. Epidermal electronics. *Science* **333**, 838–843 (2011).
8. Lipani, L. et al. Non-invasive, transdermal, path-selective and specific glucose monitoring via a graphene-based platform. *Nat. Nanotechnol.* **13**, 504–511 (2018).
9. Chen, G.-Z., Chan, I.-S. & Lam, D. C. C. Capacitive contact lens sensor for continuous non-invasive intraocular pressure monitoring. *Sens. Actuators A* **203**, 112–118 (2013).
10. Casson, R. J., Chidlow, G., Wood, J. P., Crowston, J. G. & Goldberg, I. Definition of glaucoma: clinical and experimental concepts. *Clin. Exp. Ophthalmol.* **40**, 341–349 (2012).
11. Moraes, C. G. V. D. et al. Risk factors for visual field progression in treated glaucoma. *Arch. Ophthalmol.* **129**, 562–568 (2011).
12. Renard, E. et al. Twenty-four hour (nyctohemeral) rhythm of intraocular pressure and ocular perfusion pressure in normal-tension glaucoma. *Invest. Ophthalmol. Vis. Sci.* **51**, 882–889 (2010).
13. Ku, M. et al. Smart, soft contact lens for wireless immunosensing of cortisol. *Sci. Adv.* **6**, eabb2891 (2020).
14. Moses, R. A. The Goldmann applanation tonometer. *Am. J. Ophthalmol.* **46**, 865–869 (1958).
15. Muir, K. W. Home tonometry—can we? should we? *JAMA Ophthalmol.* **135**, 1036 (2017).
16. Hom, M. & Bruce, A. *Manual of Contact Lens Prescribing and Fitting with CD-ROM* 3rd edn (Butterworth-Heinemann, 2006).
17. Flatau, A. et al. Measured changes in limbal strain during simulated sleep in face down position using an instrumented contact lens in healthy adults and adults with glaucoma. *JAMA Ophthalmol.* **134**, 375–382 (2016).
18. Leonardi, M., Pitchon, E. M., Bertsch, A., Renaud, P. & Mermoud, A. Wireless contact lens sensor for intraocular pressure monitoring: assessment on enucleated pig eyes. *Acta Ophthalmol.* **87**, 433–437 (2009).
19. Liao, Y. T., Yao, H., Lingley, A., Parviz, B. & Otis, B. P. A 3-μW CMOS glucose sensor for wireless contact-lens tear glucose monitoring. *IEEE J. Solid State Circuits* **47**, 335–344 (2012).
20. Piso, D., Veiga-Crespo, P. & Vecino, E. Modern monitoring intraocular pressure sensing devices based on application specific integrated circuits. *J. Biomater. Nanobiotechnol* **3**, 301–309 (2012).
21. Pandey, J. et al. A fully integrated RF-powered contact lens with a single element display. *IEEE Trans. Biomed. Circuits Syst.* **4**, 454–461 (2010).
22. Kim, J. et al. Wearable smart sensor systems integrated on soft contact lenses for wireless ocular diagnostics. *Nat. Commun.* **8**, 14997 (2017).
23. Dunbar, G. E., Shen, B. Y. & Aref, A. A. The sensimed triggerfish contact lens sensor: efficiency, safety, and patient perspectives. *Clin. Ophthalmol.* **11**, 875–882 (2017).
24. Park, J. et al. Soft, smart contact lenses with integrations of wireless circuits, glucose sensors, and displays. *Sci. Adv.* **4**, eaap9841 (2018).
25. Romeo, A., Liu, Q., Suo, Z. & Lacour, S. P. Elastomeric substrates with embedded stiff platforms for stretchable electronics. *Appl. Phys. Lett.* **102**, 131904 (2013).
26. Robinson, A., Aziz, A., Liu, Q., Suo, Z. & Lacour, S. P. Hybrid stretchable circuits on silicone substrate. *J. Appl. Phys.* **115**, 143511 (2014).
27. Hjortdal, J. Ø. & Jensen, P. K. In vitro measurement of corneal strain, thickness, and curvature using digital image processing. *Acta Ophthalmol. Scand.* **73**, 5–11 (1995).
28. Leonardi, M., Leuenberger, P., Bertrand, D., Bertsch, A. & Renaud, P. First steps toward noninvasive intraocular pressure monitoring with a sensing contact lens. *Invest. Ophthalmol. Vis. Sci.* **45**, 3113–3117 (2004).
29. Douthwaite, W. A. & Lam, A. K. C. The effect of an artificially elevated intraocular pressure on the central corneal curvature. *Ophthalmic Physiol. Opt.* **17**, 18–24 (1997).
30. Tadakaluru, S., Thongwusan, W. & Singjai, P. Stretchable and flexible high-strain sensors made using carbon nanotubes and graphite films on natural rubber. *Sensors* **14**, 868–876 (2014).
31. Yamada, T. et al. A stretchable carbon nanotube strain sensor for human-motion detection. *Nat. Nanotechnol.* **6**, 296–301 (2011).
32. Amjadi, M., Pichitpajongkit, A., Lee, S., Ryu, S. & Park, I. Highly stretchable and sensitive strain sensor based on silver nanowire-elastomer nanocomposite. *ACS Nano* **8**, 5154–5163 (2014).
33. Gong, S. et al. Highly stretchy black gold e-skin nanopatches as highly sensitive wearable biomedical sensors. *Adv. Electron. Mater.* **1**, 1400063 (2015).
34. Yang, S. & Lu, N. Gauge factor and stretchability of silicon-on-polymer strain gauges. *Sensors* **13**, 8577–8594 (2013).
35. Kim, D.-H. et al. Electronic sensor and actuator webs for large-area complex geometry cardiac mapping and therapy. *Proc. Natl Acad. Sci. USA* **109**, 19910–19915 (2012).
36. Hoffmann, E. M., Grus, F.-H. & Pfeiffer, N. Intraocular pressure and ocular pulse amplitude using dynamic contour tonometry and contact lens tonometry. *BMC Ophthalmol.* **4**, 4 (2004).
37. Lee, J. O. et al. A microscale optical implant for continuous in vivo monitoring of intraocular pressure. *Microsyst. Nanoeng.* **3**, 17057 (2017).
38. Kim, K. H., Lee, J. O., Du, J., Sretavan, D. & Choo, H. Real-time in vivo intraocular pressure monitoring using an optomechanical implant and an artificial neural network. *IEEE Sens. J.* **17**, 7394–7404 (2018).
39. Kim, J. et al. Epidermal electronics with advanced capabilities in near-field communication. *Small* **11**, 906–912 (2015).
40. Kim, J. et al. Miniaturized flexible electronic systems with wireless power and near-field communication capabilities. *Adv. Funct. Mater.* **25**, 4761–4767 (2015).
41. Tao, H. et al. Silk-based conformal, adhesive, edible food sensors. *Adv. Mater.* **24**, 1067–1072 (2012).
42. Cheng, S. & Wu, Z. Microfluidic, reversibly stretchable, large-area wireless strain sensor. *Adv. Funct. Mater.* **21**, 2282–2290 (2011).
43. Kim, J. et al. Highly transparent and stretchable field-effect transistor sensors using graphene–nanowire hybrid nanostructures. *Adv. Mater.* **27**, 3292–3297 (2015).
44. Mujal, J. et al. Inkjet printed antennas for NFC systems. In *Proc. 17th IEEE International Conference on Electronics, Circuits and Systems* 1220–1223 (IEEE, 2010).
45. Li, S., Sun, F., An, D. & He, S. Increasing efficiency of a wireless energy transfer system by spatial translational transformation. *IEEE Trans. Power Electron.* **99**, 3325–3332 (2017).
46. Ladd, C., So, J.-H., Muth, J. & Dickey, M. D. 3D printing of free standing liquid metal microstructures. *Adv. Mater.* **25**, 5081–5085 (2013).
47. *IEEE Standard for Safety Levels with Respect to Human Exposure to Radio Frequency Electromagnetic Fields, 3 kHz to 300 GHz* IEEE Std C95.1-2005 (Revision of IEEE Std C95.1-1991), 1–238 (IEEE, 2006).
48. *Standard Guide for Accelerated Aging of Sterile Barrier Systems for Medical Devices* ASTM F1980-07 (American Society for Testing Materials, 2011).
49. Efron, N. Grading scales for contact lens complications. *Ophthalmic Physiol. Opt.* **18**, 182–186 (1998).
50. First, P. G. et al. The influence of soft contact lenses on the intraocular pressure measurement. *Eye* **26**, 278–282 (2012).
51. Realini, T., Weinreb, R. N. & Wisniewski, S. R. Diurnal intraocular pressure patterns are not repeatable in the short-term in healthy individuals. *Ophthalmology* **117**, 1700–1704 (2010).
52. Kim, J. et al. Dataset for 'A soft and transparent contact lens for the wireless quantitative monitoring of intraocular pressure'. *Figshare* <https://doi.org/10.6084/m9.figshare.13289342> (2020).

Acknowledgements

This work was supported by the Ministry of Science & ICT (MSIT) and the Ministry of Trade, Industry and Energy (MOTIE) of Korea through the National Research Foundation (2019R1A2B5B03069358 and 2016R1A5A1009926), the Bio & Medical Technology Development Program (2018M3A9F1021649), the Nano Material Technology Development Program (2016M3A7B4910635) and the Technology Innovation Program (20010366 and 20013621, Center for Super Critical Material Industrial Technology). We also acknowledge financial support from the Institute for Basic Science (IBS-R026-D1), the Research Program (2019-22-0228) and the Post Doc Researcher Supporting program of 2019 (2019-12-0010) funded by Yonsei University.

Author contributions

Joohee Kim and J.P. carried out the experiments, analysed the data and wrote the manuscript. Y.-G.P. performed the experiments related to the printing of stretchable 3D interconnects. E.C. and M.K. performed the fabrication of contact lenses. H.S.A. participated in the design of stretchable antennas. K.-P.L. and M.-I.H. participated in the in vivo experiments. Junmo Kim and T.-S.K. performed the DIC experiments. D.W.K., H.K.K. and J.-U.P. oversaw all of the research phases and revised the manuscript. All of the authors discussed and commented on the manuscript.

Competing interests

The authors declare no competing interests.

Additional information

Supplementary information The online version contains supplementary material available at <https://doi.org/10.1038/s41551-021-00719-8>.

Correspondence and requests for materials should be addressed to D.W.K., H.K.K. or J.-U.P.

Peer review information *Nature Biomedical Engineering* thanks the anonymous reviewers for their contribution to the peer review of this work.

Reprints and permissions information is available at www.nature.com/reprints.

Publisher's note Springer Nature remains neutral with regard to jurisdictional claims in published maps and institutional affiliations.

© The Author(s), under exclusive licence to Springer Nature Limited 2021

Reporting Summary

Nature Research wishes to improve the reproducibility of the work that we publish. This form provides structure for consistency and transparency in reporting. For further information on Nature Research policies, see our [Editorial Policies](#) and the [Editorial Policy Checklist](#).

Statistics

For all statistical analyses, confirm that the following items are present in the figure legend, table legend, main text, or Methods section.

n/a Confirmed

- The exact sample size (n) for each experimental group/condition, given as a discrete number and unit of measurement
- A statement on whether measurements were taken from distinct samples or whether the same sample was measured repeatedly
- The statistical test(s) used AND whether they are one- or two-sided
Only common tests should be described solely by name; describe more complex techniques in the Methods section.
- A description of all covariates tested
- A description of any assumptions or corrections, such as tests of normality and adjustment for multiple comparisons
- A full description of the statistical parameters including central tendency (e.g. means) or other basic estimates (e.g. regression coefficient) AND variation (e.g. standard deviation) or associated estimates of uncertainty (e.g. confidence intervals)
- For null hypothesis testing, the test statistic (e.g. F , t , r) with confidence intervals, effect sizes, degrees of freedom and P value noted
Give P values as exact values whenever suitable.
- For Bayesian analysis, information on the choice of priors and Markov chain Monte Carlo settings
- For hierarchical and complex designs, identification of the appropriate level for tests and full reporting of outcomes
- Estimates of effect sizes (e.g. Cohen's d , Pearson's r), indicating how they were calculated

Our web collection on [statistics for biologists](#) contains articles on many of the points above.

Software and code

Policy information about [availability of computer code](#)

Data collection Microsoft Excel 2018
ANSYS HFSS 18.0
Android Studio 3.6

Data analysis SPSS statistics program 20
ABAQUS 6.13
Origin Pro 2015 (Origin Lab)
FLIR ResearchIR software 4 (Research IR Max, FLIR systems)
DIC algorithm program 1.2 (ARAMIS, GOM, Germany)

For manuscripts utilizing custom algorithms or software that are central to the research but not yet described in published literature, software must be made available to editors and reviewers. We strongly encourage code deposition in a community repository (e.g. GitHub). See the Nature Research [guidelines for submitting code & software](#) for further information.

Data

Policy information about [availability of data](#)

All manuscripts must include a [data availability statement](#). This statement should provide the following information, where applicable:

- Accession codes, unique identifiers, or web links for publicly available datasets
- A list of figures that have associated raw data
- A description of any restrictions on data availability

The rabbit in vivo data are available in figshare with the identifier doi:10.6084/m9.figshare.13289342. The human data are available within the paper and its

supplementary information. The raw and analysed datasets generated for the studies shown in Figs. 1–3 are available for research purposes from the corresponding authors on reasonable request.

Field-specific reporting

Please select the one below that is the best fit for your research. If you are not sure, read the appropriate sections before making your selection.

Life sciences Behavioural & social sciences Ecological, evolutionary & environmental sciences

For a reference copy of the document with all sections, see nature.com/documents/nr-reporting-summary-flat.pdf

Life sciences study design

All studies must disclose on these points even when the disclosure is negative.

Sample size	No sample-size calculations were performed, because the goal of this study was to demonstrate new methodology. There were no major hypotheses tested.
Data exclusions	No data were excluded from the analyses.
Replication	At least three biologically independent experiments were performed in each case.
Randomization	All devices tested were selected randomly.
Blinding	The investigators were blinded to group allocation during data collection and analysis.

Reporting for specific materials, systems and methods

We require information from authors about some types of materials, experimental systems and methods used in many studies. Here, indicate whether each material, system or method listed is relevant to your study. If you are not sure if a list item applies to your research, read the appropriate section before selecting a response.

Materials & experimental systems

n/a	Involved in the study
<input checked="" type="checkbox"/>	Antibodies
<input checked="" type="checkbox"/>	Eukaryotic cell lines
<input checked="" type="checkbox"/>	Palaeontology and archaeology
<input type="checkbox"/>	Animals and other organisms
<input type="checkbox"/>	Human research participants
<input checked="" type="checkbox"/>	Clinical data
<input checked="" type="checkbox"/>	Dual use research of concern

Methods

n/a	Involved in the study
<input checked="" type="checkbox"/>	ChIP-seq
<input checked="" type="checkbox"/>	Flow cytometry
<input checked="" type="checkbox"/>	MRI-based neuroimaging

Animals and other organisms

Policy information about [studies involving animals](#); [ARRIVE guidelines](#) recommended for reporting animal research

Laboratory animals	New Zealand White rabbits (male, 8–12 weeks, 2.0–3.0 kg), were purchased from the Hyochang Science (Republic of Korea).
Wild animals	The study did not involve wild animals.
Field-collected samples	The study did not involve samples collected from the field.
Ethics oversight	The animal experiments were performed under IACUC approval (UNISTIACUC-18-02, DGMIF-18041703-00, and IACUCA-201908-945-02).

Note that full information on the approval of the study protocol must also be provided in the manuscript.

Human research participants

Policy information about [studies involving human research participants](#)

Population characteristics	The participants were healthy subjects.
Recruitment	One participant in the experiments was one of the investigators, who volunteered to be a subject. The other participants

Recruitment

were recruited by the Department of Materials Science Engineering at UNIST. There were no self-selection biases or other biases.

Ethics oversight

The human study was performed after IRB approval (UNISTIRB-18-17-A).

Note that full information on the approval of the study protocol must also be provided in the manuscript.